

Structural analysis and transport properties of [010]-tilt grain boundaries in Fe(Se,Te)

Kazumasa Iida^{a,b}, Yoshihiro Yamauchi^c, Takafumi Hatano^{b,c}, Kai Walter^d, Bernhard Holzapfel^d, Jens Hänisch^d, Zimeng Guo^{b,e}, Hongye Gao^f, Haoshan Shi^g, Shinnosuke Tokuta^{b,h}, Satoshi Hata^{b,e,f,g}, Akiyasu Yamamoto^{b,h} and Hiroshi Ikuta^{c,i}

^aCollege of Industrial Technology, Nihon University, Narashino, Chiba, Japan;

^bJST CREST, Kawaguchi, Saitama, Japan;

^cDepartment of Materials Physics, Nagoya University, Nagoya, Japan;

^dInstitute for Technical Physics, Karlsruhe Institute of Technology, Eggenstein-Leopoldshafen, Germany;

^eDepartment of Advanced Materials Science and Engineering, Kyushu University, Kasuga, Fukuoka, Japan;

^fThe Ultramicroscopy Research Center, Kyushu University, Fukuoka, Japan;

^gInterdisciplinary Graduate School of Engineering Sciences, Kyushu University, Kasuga, Fukuoka, Japan;

^hDepartment of Applied Physics, Tokyo University of Agriculture and Technology, Koganei, Tokyo, Japan;

ⁱResearch Center for Crystalline Materials Engineering, Nagoya University, Nagoya, Japan

ABSTRACT

Understanding the nature of grain boundaries is a prerequisite for fabricating high-performance superconducting bulks and wires. For iron-based superconductors [e.g. Ba(Fe,Co)₂As₂, Fe(Se,Te), and NdFeAs(O,F)], the dependence of the critical current density J_c on misorientation angle (θ_{GB}) has been explored on [001]-tilt grain boundaries, but no data for other types of orientations have been reported. Here, we report on the structural and transport properties of Fe(Se,Te) grown on CeO₂-buffered symmetric [010]-tilt roof-type SrTiO₃ bicrystal substrates by pulsed laser deposition. X-ray diffraction and transmission electron microscopy revealed that θ_{GB} of Fe(Se,Te) was smaller whereas θ_{GB} of CeO₂ was larger than that of the substrate. The difference in θ_{GB} between the CeO₂ buffer layer and the substrate is getting larger with increasing θ_{GB} . For $\theta_{GB} \geq 24^\circ$ of the substrates, θ_{GB} of Fe(Se,Te) was zero, whereas θ_{GB} of CeO₂ was continuously increasing. The inclined growth of CeO₂ can be explained by the geometrical coherency model. The *c*-axis growth of Fe(Se,Te) for $\theta_{GB} \geq 24^\circ$ of the substrates is due to the domain matching epitaxy on {221} planes of CeO₂. Electrical transport measurements confirmed no reduction of inter-grain J_c for $\theta_{GB} \leq 9^\circ$, indicative of strong coupling between the grains.

ARTICLE HISTORY

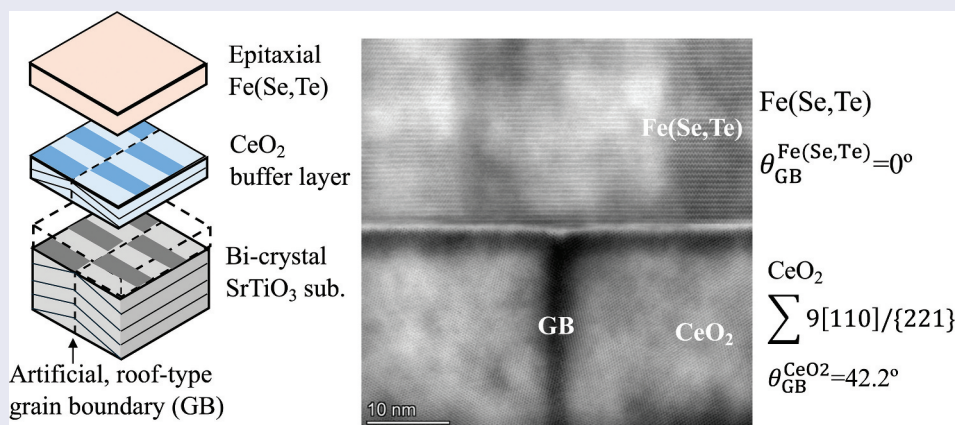
Received 2 May 2024

Accepted 21 July 2024

Revised 30 June 2024

KEYWORDS

Fe(Se,Te); roof-type grain boundary; domain matching epitaxy





IMPACT STATEMENT


The issue of weak-links inherent in iron-based superconductors, Fe(Se,Te), can be avoided by employing CeO₂-buffer layer containing the $\Sigma 9[110]/\{221\}$ grain boundary.

1. Introduction

Grain boundaries (GBs) are interfaces between crystalline grains at which the crystallographic

orientation abruptly changes. Microscopically, the overlap of the wave functions is perturbed by GBs,

CONTACT Kazumasa Iida  iida.kazumasa@nihon-u.ac.jp  College of Industrial Technology, Nihon University, 1-2-1 Izumi-Cho, Narashino, Chiba 275-8575, Japan

 Supplemental data for this article can be accessed online at <https://doi.org/10.1080/14686996.2024.2384829>

© 2024 The Author(s). Published by National Institute for Materials Science in partnership with Taylor & Francis Group.

This is an Open Access article distributed under the terms of the Creative Commons Attribution-NonCommercial License (<http://creativecommons.org/licenses/by-nc/4.0/>), which permits unrestricted non-commercial use, distribution, and reproduction in any medium, provided the original work is properly cited. The terms on which this article has been published allow the posting of the Accepted Manuscript in a repository by the author(s) or with their consent.

leading to a change in the electronic structure. The electronic structure is also affected by local strain and dislocations in and around the GB. Hence, physical properties across GBs are expectedly altered, and understanding the nature of GBs is therefore an important step for further improvement of the functionalities of materials. Polycrystalline samples contain many types of GBs, which complicates the investigations of specific GBs. To understand the nature of such a specific GB, they have to be fabricated artificially. For instance, the attempt at realizing artificial GBs in silicon ingots has been reported recently [1]. For high-temperature superconductors (HTS, e.g. $\text{YBa}_2\text{Cu}_3\text{O}_{7-\delta}$, YBCO) as well as iron-based superconductors (IBSs), thin films containing a well-defined single GB have been fabricated, since the critical current would be too large to evaluate by electrical transport measurements on bulk samples. In this case, superconducting thin films have been grown biaxially on bicrystal substrates, which consist of two single crystals having a, usually common symmetric, rotation along [001] that are joined by a solid-state reaction [2]. After growth, the electrical transport properties across the GB are investigated as a function of misorientation angle. Such experiments are recognized as a powerful method for understanding the GB properties of HTS, for reviews see [3,4].

For cuprates, not only GBs with in-plane misorientation ([001]-tilt GB) but also with out-of-plane misorientation ([010]-tilt GB) as well as [100]- and [001]-twist GBs have been realized [5,6]. The inter-grain J_c across [001]-tilt GBs was shown to decrease exponentially above a θ_{GB} around $3^\circ \sim 5^\circ$ [2,3,5]. This angle is defined as the critical angle θ_c . Similar to the [001]-tilt GBs, the inter-grain J_c reduced significantly at the [100]-twist type GBs. On the other hand, the inter-grain J_c of [001]-twist GBs for $\text{Bi}_2\text{Sr}_2\text{CaCu}_2\text{O}_{8+\delta}$ was unaltered regardless of misorientation angle [7]. For YBCO, the inter-grain J_c of [010]-tilt GBs was almost constant even for $\theta_{\text{GB}} = 8^\circ$ [5,6], indicating that θ_c can depend on the type of GB.

For $\text{Ba}(\text{Fe},\text{Co})_2\text{As}_2$ [8], $\text{Fe}(\text{Se},\text{Te})$ [9,10], and $\text{NdFeAs}(\text{O},\text{F})$ [11,12], only [001]-tilt GBs have been investigated so far. The common feature of those IBSs is that θ_c is around 9° , which is 2–3 times larger than for YBCO of the same type of GB. Additionally, the inter-grain J_c stayed constant in the range $15^\circ \leq \theta_{\text{GB}} \leq 45^\circ$, whereas for YBCO it decreases further exponentially with θ_{GB} . These prominent features of GBs in IBSs may originate from their $s \pm$ wave symmetry. However, no data for other types of orientations have been reported. Hence, it is interesting how J_c is affected by [010]-tilt as well as twist GBs. To address this issue, we have fabricated $\text{Fe}(\text{Se},\text{Te})$ thin films on symmetric [010]-tilt roof-type SrTiO_3 bicrystals with θ_{GB} up to

30° and investigated the structural and transport properties.

We have selected $\text{Fe}(\text{Se},\text{Te})$, since it has the simplest crystal structure among IBSs. Hence, it is considered easy to extract the factors governing the superconducting properties. However, growing $\text{Fe}(\text{Se},\text{Te})$ thin films with good superconducting properties is not easy due to the excess Fe, which localizes conducting carriers, leading to a lower J_c [13]. In fact, as-grown films under our growth conditions contain excess Fe.

In this paper, we firstly optimize the post-annealing conditions for $\text{Fe}(\text{Se},\text{Te})$ to remove excess Fe. Then, $\text{Fe}(\text{Se},\text{Te})$ bicrystal films are fabricated by employing the optimized post-annealing condition, followed by structural and electrical transport characterizations.

2. Experiment

CeO_2 was grown on $\text{SrTiO}_3(001)$ (K&R Creation Co., Ltd. Japan) in $p\text{O}_2 = 1 \text{ Pa}$ at 600°C by pulsed laser deposition (PLD), where a commercially available CeO_2 sintered target (Toshima Manufacturing Co., Ltd. Japan) was ablated by a KrF excimer laser (COMPex 102F, Coherent Inc., USA) (wavelength $\lambda = 248 \text{ nm}$) with 1 Hz. An energy density of $\sim 1.2 \text{ J}/\text{cm}^2$ at the target surface was employed. A total pulse number of 1320 yielded a 30 nm-thick CeO_2 film confirmed by X-ray reflectivity measurements (Supplementary Figure S1). After deposition, the CeO_2 -buffered SrTiO_3 substrates were transferred to the UHV chamber (base pressure $\sim 1 \times 10^{-7} \text{ Pa}$) for deposition of $\text{Fe}(\text{Se},\text{Te})$ without exposing them to air. The $\text{Fe}(\text{Se},\text{Te})$ target with nominal composition $\text{Fe}:\text{Se}:\text{Te} = 1:0.5:0.5$ was prepared by spark plasma sintering [14]. The precursor powders were mechanically alloyed prior to the sintering [15]. The nominal $\text{FeSe}_{0.5}\text{Te}_{0.5}$ films were also grown on CeO_2 -buffered [010]-tilt roof-type SrTiO_3 bicrystal substrates ($8^\circ \leq \theta_{\text{GB}}^{\text{STO}} \leq 30^\circ$, Furuuchi Chemical Co., Japan) at 300°C and with 5 Hz laser repetition rate. The energy density of the laser was the same as for the CeO_2 deposition. A pulse number of 7500 yielded a 135–155 nm-thick $\text{FeSe}_{0.5}\text{Te}_{0.5}$ layer, which is the optimum thickness for achieving a high T_c [16,17].

Post annealing has been conducted by referring to [18,19]. The samples were again transferred to the CeO_2 deposition chamber after growth of $\text{FeSe}_{0.5}\text{Te}_{0.5}$ followed by annealing at $100^\circ\text{C} \leq T_{\text{anneal}} \leq 350^\circ\text{C}$ in a fixed $p\text{O}_2$ of 1 Pa. The dwell time at the maximum T_{anneal} for each experimental run was fixed at 10 min.

Structural properties of the films were characterized by X-ray diffraction (XRD, RINT2000 and ULTIMA IV, RIGAKU, Japan) using $\text{Cu K}\alpha$ radiation and transmission electron microscopy (TEM). The [001] directions of both $\text{FeSe}_{0.5}\text{Te}_{0.5}$ and CeO_2 are expected to be away from the substrate normal by $\theta_{\text{GB}}^{\text{STO}}/2$ when $\text{FeSe}_{0.5}\text{Te}_{0.5}$ is

grown on CeO_2 -buffered symmetric [010]-tilt SrTiO_3 bicrystal substrates having $\theta_{\text{GB}}^{\text{STO}}$. Hence, the growth angles (i.e. offset angles) for $\text{FeSe}_{0.5}\text{Te}_{0.5}$ and CeO_2 were determined by ω -scans, where the angle 2θ was fixed to the 002 reflections of each layer. TEM was performed on a cross-sectional foil sample covering the grain boundary. The foil sample was made by focused ion beam (FIB) in a scanning electron microscope (SEM) called Helios Hydra CX (Thermo Fisher Sci., USA). The scanning TEM (STEM) observations were carried out for high-resolution microstructural analyses by a TEM called Titan Cubed G2 (Thermo Fisher Sci., USA). In order to accurately assess the grain boundary angle in each layer, the automated crystal orientation mapping (ACOM) technique in a TEM called ARM-200F (JEOL Ltd., Japan) was performed by using ASTAR device (NanoMEGAS, Belgium) with a spatial resolution of 4 nm and an acceleration voltage of 200 kV. Details of the ACOM in TEM are described in refs. [20,21].

After structural characterization, electrical transport properties were measured using a 4-probe method on micro-bridges fabricated by laser cutting (UV-MK-kit, Kokyo, Inc., Japan). The bridges of 100 μm width had a length of 2 mm for inter-grain measurements, and 1 mm for intra-grain measurements, respectively. The superconducting transition temperature ($T_{c,90}$) was defined as a 10% drop of the normal state resistance R_n , at which the resistance deviated from the linear fit to the normal state in the vicinity of the superconducting transition. J_c was determined by an electrical field criterion of 1 $\mu\text{V}/\text{cm}$.

3. Results and discussion

3.1. Removal of excess Fe

The as-grown $\text{FeSe}_{0.5}\text{Te}_{0.5}$ films on CeO_2 -buffered ordinary $\text{SrTiO}_3(001)$ substrates contained excess Fe,

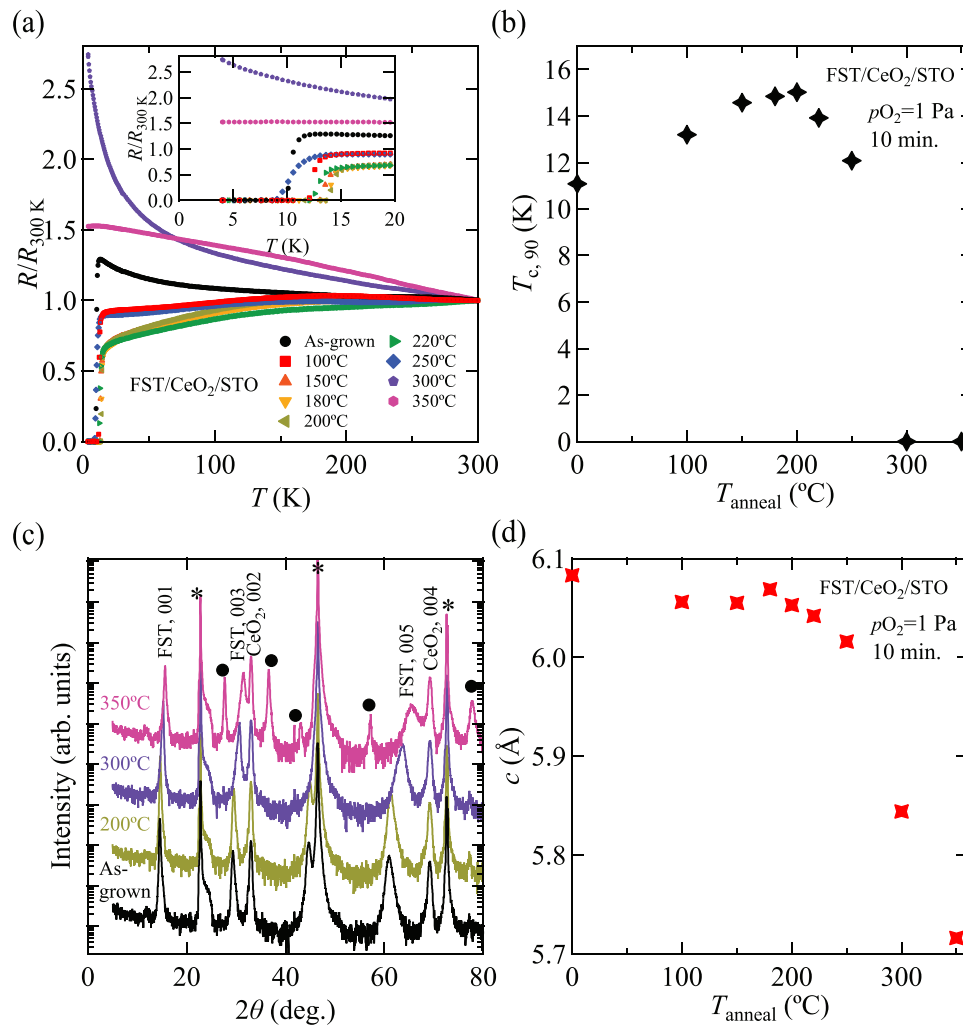


Figure 1. (a) The resistance curves of the as-grown $\text{FeSe}_{0.5}\text{Te}_{0.5}$ (FST) and the FST films annealed at various temperatures normalized to the value at 300 K. Inset shows a magnified image of (a) around the superconducting transition. STO represents the SrTiO_3 substrate. (b) The transition temperature $T_{c,90}$ as a function of the annealing temperature T_{anneal} . The maximum $T_{c,90}$ around 15 K was observed at $T_{\text{anneal}} = 200^\circ\text{C}$. (c) The XRD patterns of the $\text{FeSe}_{0.5}\text{Te}_{0.5}$ thin films annealed at 200°C, 300°C, and 350°C. For comparison, the data for the as-grown film is also shown. Beyond the optimum T_{anneal} , the 00/ diffraction peaks shifted to higher angles. For $T_{\text{anneal}} = 350^\circ\text{C}$, some diffraction peaks marked as "•" other than FST and CeO_2 were observed. The peaks marked as "*" originate from SrTiO_3 . (d) The c -axis length as a function of the annealing temperature T_{anneal} . The c -axis length of the superconducting films was located between 6.0 Å and 6.1 Å.

inferred from a resistance upturn before the superconducting transition (Figure 1(a)). This upturn is due to the charge carrier localization by excess Fe in Fe(Se,Te) [13]. Figure 1(a) shows the normalized resistance curves of the FeSe_{0.5}Te_{0.5} thin films after post-annealing. The resistance upturn was gradually suppressed with increasing T_{anneal} . At $200^{\circ}\text{C} \leq T_{\text{anneal}} \leq 220^{\circ}\text{C}$, the upturn disappeared. Simultaneously, the superconducting transition temperature $T_{c,90}$ increased with T_{anneal} and reached a maximum around 15 K at $T_{\text{anneal}} = 200^{\circ}\text{C}$ (Figure 1(b)). Further increasing T_{anneal} reduced $T_{c,90}$. For $T_{\text{anneal}} > 300^{\circ}\text{C}$, superconductivity disappeared completely. Additionally, the resistance curve for the film annealed at 300°C showed semiconducting behavior. Figure 1(c) shows the XRD patterns of FeSe_{0.5}Te_{0.5} annealed at various temperatures. In the XRD $2\theta/\omega$ scans, no appreciable differences between the as-grown film and the film annealed at 200°C were observed. On the other hand, significant shifts of the $00l$ reflections toward higher 2θ values were observed for the film annealed at 300°C , indicative of a decrease in c -axis length. This is mainly due to the loss of Te, since severe annealing conditions may terminate the Fe-Te bonds leading to a loss in Te [22] and the c -axis length is decreasing with decreasing Te content in FeSe_{0.5}Te_{0.5} single crystal [23]. When the film was annealed at 350°C , further shifting of the $00l$ peaks together with peaks originating from impurities was recognized. In fact, the c -axis length significantly reduced at $T_{\text{anneal}} \geq 300^{\circ}\text{C}$ (Figure 1(d)), whereas the c -axis length of the superconducting films located between 6.0 Å and 6.1 Å. From those results, the optimum post-annealing temperature was determined as 200°C .

The post-annealing conditions in this study differed from the ones reported by Zhang et al. [18] with respect to $p\text{O}_2$, annealing temperature and

dwell time, which were there 100 mbar (~ 13.3 Pa), 90°C and $1\sim 2$ h. The annealing temperature of 200°C in our case is almost the double of Zhang's study, whereas our dwell time is shorter. In our study, the resistance upturn was suppressed even at $T_{\text{anneal}} = 100^{\circ}\text{C}$. Hence, it may be possible to remove more Fe with further increasing the holding time. The post-annealing reported by Zhang *et al.* not only led to removal of excess Fe but also to a significant enhancement of critical currents, although T_c was slightly reduced. Post-annealing at low temperatures may indeed be used to tune the properties of superconducting films further, such as critical current properties of REBCO films [24]. Nevertheless, in the following, the FeSe_{0.5}Te_{0.5} films on CeO₂-buffered [010]-tilt SrTiO₃ bicrystal substrates were post-annealed at 200°C for 10 min in 1 Pa of oxygen.

3.2. Structural analyses

Figure 2(a) exhibits the XRD $2\theta/\omega$ patterns of FeSe_{0.5}Te_{0.5} grown on CeO₂-buffered [010]-tilt SrTiO₃ bicrystal substrates with various misorientation angles. The film for $\theta_{\text{GB}}^{\text{STO}} = 0^{\circ}$ was grown on an ordinary SrTiO₃(001) substrate. The angle $\theta_{\text{GB}}^{\text{FST}}$ shown in the panel indicates the measured offset angle of FeSe_{0.5}Te_{0.5} multiplied by two [i.e. the actual misorientation angle of FeSe_{0.5}Te_{0.5}], and the angle in parenthesis is the misorientation angle of the SrTiO₃ bicrystals ($\theta_{\text{GB}}^{\text{STO}}$). For $\theta_{\text{GB}}^{\text{STO}} = 0^{\circ}$, the $00l$ reflections of FeSe_{0.5}Te_{0.5} and CeO₂ together with SrTiO₃ were observed. Additionally, the 101 reflection of the ϕ scan showed a fourfold symmetry [Supplementary Figure S2(a)], which proves the phase-pure and epitaxial growth of FeSe_{0.5}Te_{0.5}.

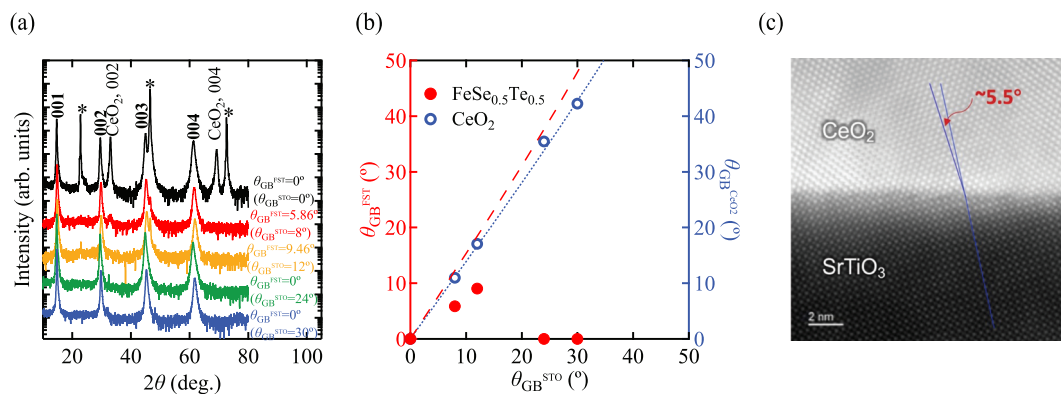


Figure 2. (a) The XRD pattern of the FeSe_{0.5}Te_{0.5} thin films grown on CeO₂-buffered [010]-tilt symmetric SrTiO₃ (STO) bicrystal substrates having various grain boundary angles $\theta_{\text{GB}}^{\text{STO}}$. Here, the angle $\theta_{\text{GB}}^{\text{FST}}$ corresponds to twice the offset angle of FeSe_{0.5}Te_{0.5}. The peaks marked “*” originate from SrTiO₃. Because of the different offset angles between FeSe_{0.5}Te_{0.5} and CeO₂ as well as FeSe_{0.5}Te_{0.5} and SrTiO₃, almost only the $00l$ peaks from FeSe_{0.5}Te_{0.5} were observed. (b) The $\theta_{\text{GB}}^{\text{FST}}$ for FeSe_{0.5}Te_{0.5} (closed symbol) and $\theta_{\text{GB}}^{\text{CeO}_2}$ for CeO₂ (open symbol) as a function of $\theta_{\text{GB}}^{\text{STO}}$. The dashed red and dotted blue lines are calculations using the geometrical coherency model [25–27]. (c) The atomic resolution HAADF-STEM image of the interface between CeO₂ and SrTiO₃ having a $\theta_{\text{GB}}^{\text{STO}} = 30^{\circ}$. The calculated value of $(\theta_{\text{GB}}^{\text{CeO}_2} - \theta_{\text{GB}}^{\text{STO}})/2$ is 5.9° , which is close to the measured value of $\sim 5.5^{\circ}$.

On the other hand, almost only the $00l$ reflections of $\text{FeSe}_{0.5}\text{Te}_{0.5}$ were observed for $\theta_{\text{GB}}^{\text{STO}} > 0^\circ$, indicating that the offset angle of $\text{FeSe}_{0.5}\text{Te}_{0.5}$ differs from those of CeO_2 and SrTiO_3 . In fact, the respective misorientation angles of $\text{FeSe}_{0.5}\text{Te}_{0.5}$ and CeO_2 are different from each other and from those of the SrTiO_3 bicrystals (Figure 2(b)). As can be seen, the actual misorientation angle of CeO_2 ($\theta_{\text{GB}}^{\text{CeO}_2}$) is getting larger than $\theta_{\text{GB}}^{\text{STO}}$, whereas $\theta_{\text{GB}}^{\text{FST}}$ is always smaller than $\theta_{\text{GB}}^{\text{STO}}$. A similar effect was observed in $\text{FeSe}_{0.5}\text{Te}_{0.5}$ thin films on vicinal CaF_2 substrates deposited at 260°C [28]. For $\theta_{\text{GB}}^{\text{STO}} \geq 24^\circ$, $\theta_{\text{GB}}^{\text{FST}}$ was zero, indicating the absence of a GB in $\text{FeSe}_{0.5}\text{Te}_{0.5}$. These observations can be explained by the geometrical coherency model [25–27], according to which $\theta_{\text{GB}}^{\text{CeO}_2} - \theta_{\text{GB}}^{\text{STO}} = \Delta\theta_{\text{GB1}}$ and $\theta_{\text{GB}}^{\text{FST}} - \theta_{\text{GB}}^{\text{CeO}_2} = \Delta\theta_{\text{GB2}}$ can be calculated by

$$\frac{\Delta\theta_{\text{GB1}}}{2} = \left| \tan^{-1} \left(\frac{d_{\text{STO}} - d_{\text{CeO}_2}}{d_{\text{STO}}} \tan \frac{\theta_{\text{GB}}^{\text{STO}}}{2} \right) \right| \quad (1)$$

$$\frac{\Delta\theta_{\text{GB2}}}{2} = \left| \tan^{-1} \left(\frac{d_{\text{CeO}_2} - d_{\text{FST}}}{d_{\text{CeO}_2}} \tan \frac{\theta_{\text{GB}}^{\text{CeO}_2}}{2} \right) \right| \quad (2)$$

where d_{STO} , d_{CeO_2} , and d_{FST} are the out-of-plane, monolayer step height of SrTiO_3 (3.91 Å), CeO_2 (5.41 Å), and $\text{FeSe}_{0.5}\text{Te}_{0.5}$ (5.96 Å), respectively. The direction of the tilt of $[001]$ CeO_2 from $[001]$ SrTiO_3 is

away from the substrate normal, because $d_{\text{CeO}_2} > d_{\text{STO}}$. Similarly, the direction of the tilt of $[001]$ $\text{FeSe}_{0.5}\text{Te}_{0.5}$ from $[001]$ CeO_2 is away from the substrate normal. For $\theta_{\text{GB}}^{\text{STO}} = 30^\circ$, $\Delta\theta_{\text{GB1}}/2$ is calculated as 5.9° , which is close to the measured angle from the STEM image shown in Figure 2(c). The grain boundary angles of CeO_2 ($\theta_{\text{GB}}^{\text{CeO}_2}$) lie on the calculated (dotted blue) line (Figure 2(b)), indicating that the geometrical coherency model is valid. However, this model seems not to be valid for $\text{FeSe}_{0.5}\text{Te}_{0.5}/\text{CeO}_2$, since the experimental data did not lie on the dashed red line calculated from the model. The vicinal angles of $\text{FeSe}_{0.5}\text{Te}_{0.5}$ grown on off-cut CaF_2 substrates at 260°C deviated similarly from the calculation (Supplementary Figure S3). This may be due to the low growth temperature, leading to a low surface mobility of atoms [27]. In fact, the vicinal angles of $\text{FeSe}_{0.5}\text{Te}_{0.5}$ grown at a higher temperature of 400°C were almost identical to those of the CaF_2 substrates (Figure S3). Possibly, film surfaces and CaF_2 at low temperatures do not have well defined terraces needed for the geometry coherency mechanism. Finally, for a proper analysis, the lattice parameters at growth temperature should be considered, which we omitted here for our estimates.

Figure 3(a) shows the cross-sectional view of $\text{FeSe}_{0.5}\text{Te}_{0.5}$ grown on the CeO_2 -buffered SrTiO_3 bicrystal with $\theta_{\text{GB}}^{\text{STO}} = 30^\circ$. The respective layer thicknesses of

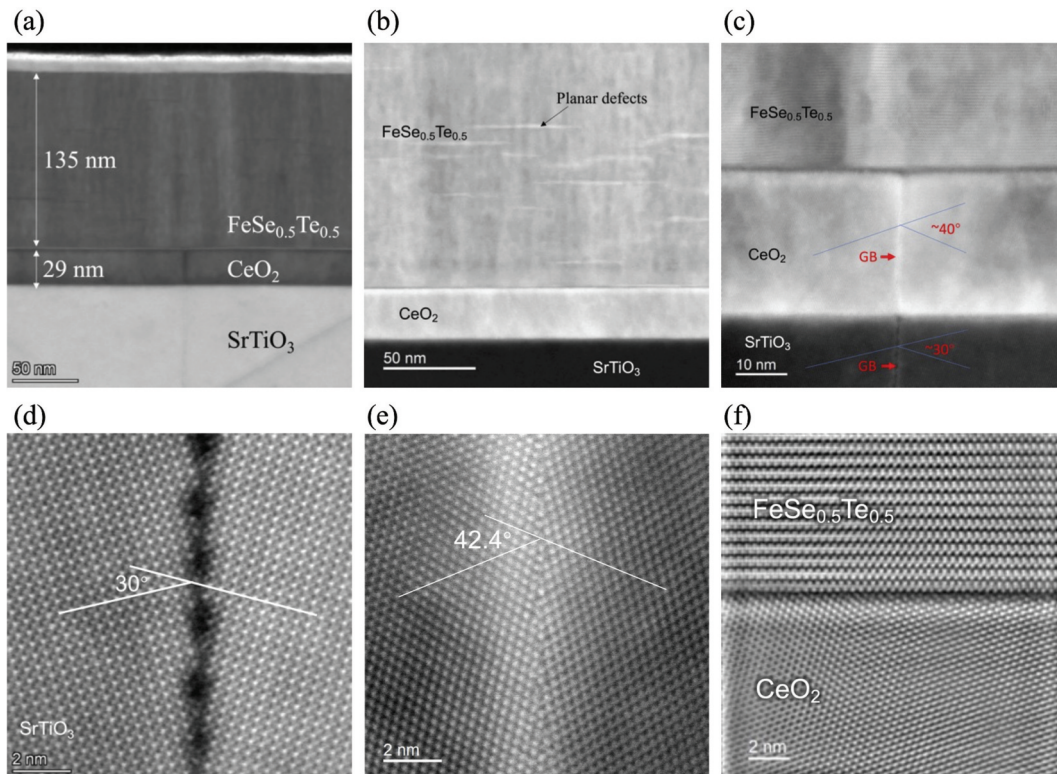


Figure 3. Microstructure of the $\text{FeSe}_{0.5}\text{Te}_{0.5}/\text{CeO}_2$ sample grown on the 30° $[010]$ -tilt symmetric SrTiO_3 bicrystal substrate. (a) Cross-sectional view near the GB acquired by ADF-STEM. (b) ADF-STEM image taken away from GB. Planar defects shown by a black arrow are visible. (c) Magnified image of (a). The GB is absent in $\text{FeSe}_{0.5}\text{Te}_{0.5}$. Atomic-resolution HAADF-STEM image of the GBs in SrTiO_3 (d) and CeO_2 (e). The GB angle in CeO_2 , $\theta_{\text{GB}}^{\text{CeO}_2}$, is 42.4° , consistent with the value by XRD. (f) Atomic-resolution image of the interface between CeO_2 and $\text{FeSe}_{0.5}\text{Te}_{0.5}$, which was clean and without reaction layer.

$\text{FeSe}_{0.5}\text{Te}_{0.5}$ and CeO_2 were 135 nm and 30 nm. The film contained planar defects with a thickness of ~ 1.5 nm along the ab -plane, Figure 3(b). Atomic-resolution images of SrTiO_3 and CeO_2 buffer layer around the GB confirmed that the respective GB angles are $\theta_{\text{GB}}^{\text{STO}} = 30^\circ$ and $\theta_{\text{GB}}^{\text{CeO}_2} = 42.4^\circ$ (Figures 3(d,e)). Those values are consistent with the ones evaluated by XRD measurements. Figure 3(c) confirms the presence of a GB in the CeO_2 buffer layer, whereas no visible GB was present in the $\text{FeSe}_{0.5}\text{Te}_{0.5}$ layer as stated above. Additionally, the $\text{FeSe}_{0.5}\text{Te}_{0.5}$ layer grew biaxially textured as shown in Figure 3(f). The in-plane texture was also confirmed by the ϕ scan of the 101 reflection [Supplementary Figure S2 (b)]. According to the geometric considerations based on the TEM observation, the epitaxial relation (001)[100] $\text{FeSe}_{0.5}\text{Te}_{0.5} \parallel (114)[22\bar{1}] \text{CeO}_2$ is realized as a domain growth [29]. In fact, a domain wall structure was observed in the $\text{FeSe}_{0.5}\text{Te}_{0.5}$ film along [010], i.e. across the GB for $\theta_{\text{GB}}^{\text{STO}} = 30^\circ$, and their average width was 32 ± 12 nm (Figures 4(a,d)). Note that such a structure has not been observed in the $\text{FeSe}_{0.5}\text{Te}_{0.5}$ film grown on CeO_2 -buffered single-crystal SrTiO_3 substrate (Supplementary Figure S4). The relation (001)[100] $\text{FeSe}_{0.5}\text{Te}_{0.5} \parallel (114)[22\bar{1}] \text{CeO}_2$ also holds for $\theta_{\text{GB}}^{\text{STO}} = 24^\circ$. Due to the extinc-

Table 1. The domain indices $C_{h,k,l}^{m,n,o}$ and the corresponding domain mismatch calculated from Equation (3).

$C_{h,k,l}^{m,n,o}$	ϵ_d (%)
$C_{1,1,0}^{2,0,0}$	-0.93
$C_{2,2,1}^{4,0,0}$	-6.82
$C_{4,4,2}^{9,0,0}$	4.96

tion rule, the diffraction peak arising from the 114 reflection of CeO_2 could not be observed in XRD pattern.

The domain growth is expressed by the following indices, $C_{h,k,l}^{m,n,o}$, where $(h \times k \times l)$ lattice of the CeO_2 buffer layer and $(m \times n \times o)$ lattice of the $\text{Fe}(\text{Se},\text{Te})$, refer to [29]. The respective indices are $C_{1,1,0}^{2,0,0}$ for along the GB and $C_{2,2,1}^{4,0,0}$ for across the GB. However, the most probable index for the latter is $C_{4,4,2}^{9,0,0}$, since the domain misfit (ϵ_d) expressed by Equation (3) is smaller, as shown in Table 1. Additionally, the domain width $9 \times a_{\text{FST}} = 34$ nm (a_{FST} : in-plane lattice parameter of $\text{FeSe}_{0.5}\text{Te}_{0.5}$) corresponds well to the average domain width of 32 nm observed in ACOM, and the opposite mismatch compared to the $\text{FeSe}_{0.5}\text{Te}_{0.5}(100)$ direction may slightly lower the total energy.

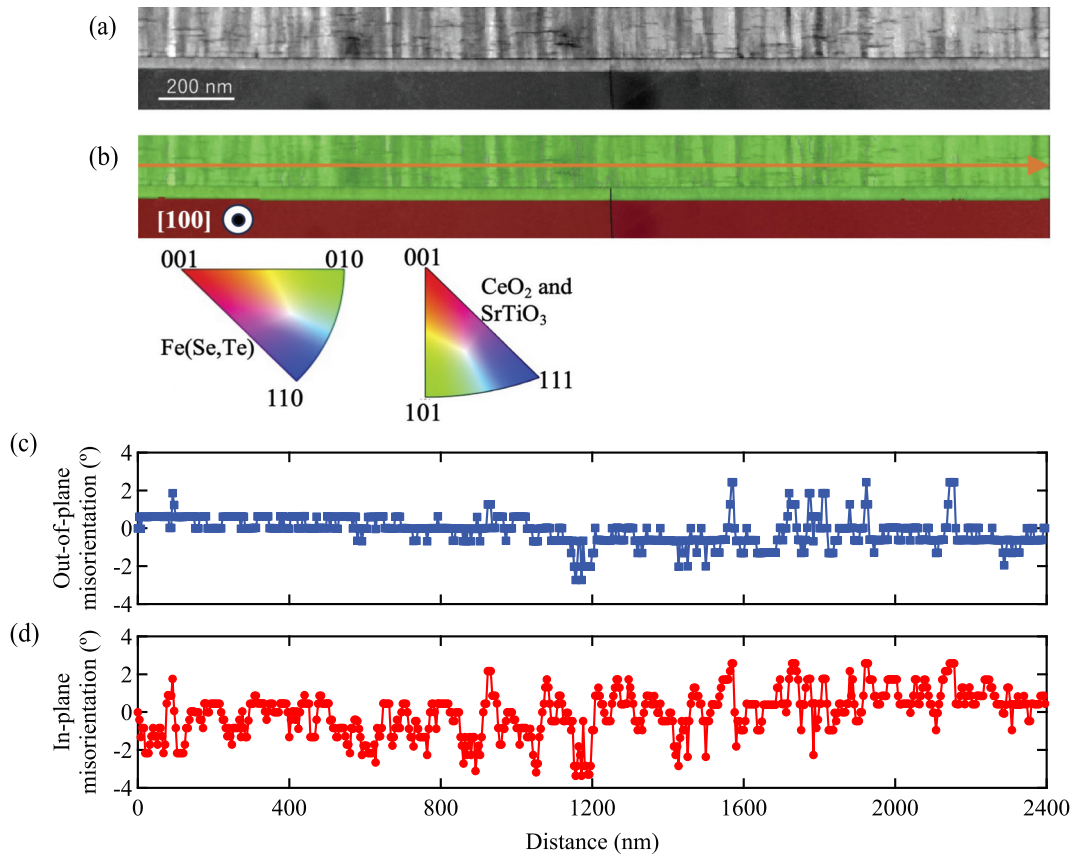


Figure 4. (a) Automatic crystal orientation mapping of $\text{FeSe}_{0.5}\text{Te}_{0.5}$ grown on CeO_2 -buffered SrTiO_3 with $\theta_{\text{GB}}^{\text{STO}} = 30^\circ$ by scanning precession diffraction. (b) Inverse pole figure map. (c) Out-of-plane and (d) in-plane misorientation profiles from the first point along the orange line shown in (b).

$$\varepsilon_d = 2 \frac{\sqrt{m^2 + n^2 + o^2} a_{\text{FST}} - \sqrt{h^2 + k^2 + l^2} a_{\text{CeO}_2}}{\sqrt{m^2 + n^2 + o^2} a_{\text{FST}} + \sqrt{h^2 + k^2 + l^2} a_{\text{CeO}_2}} \quad (3)$$

The ε_d of $C_{1,1,0}^{2,0,0}$ is smaller than that of $C_{4,4,2}^{9,0,0}$, which is reflected in the full width at half maximum values ($\Delta\omega$) of the 00 l rocking curves [Supplementary Figure S2 (h)~(k)]. As can be seen, the $\Delta\omega$ for the $[1\bar{1}0]$ (along the GB, denoted as ‘L’ in Figure S2) is smaller than that for the $[22\bar{1}]$ (across the GB, denoted as ‘T’ in Figure S2). For cubic lattices, the Σ value of symmetrical GB is expressed by the sum of the squares of the Miller indices [30]. In our experimental results, a $\Sigma 9[110]/\{221\}$ GB with an ideal GB angle of 38.9° has formed in CeO_2 on both 24° and 30° substrates with sufficiently close real GB angles of 35.4° and 42.2° , respectively. Unlike other GBs (e.g. $\Sigma 11[110]/\{332\}$), the $\Sigma 9[110]/\{221\}$ GB is, together with the twin $\Sigma 3[110]/\{111\}$ (not observed here), the most stable structure in CeO_2 [31].

Due to the difference between the ideal and real GB angle in CeO_2 (3.5° for $\theta_{\text{GB}}^{\text{STO}} = 24^\circ$ and 3.3° for $\theta_{\text{GB}}^{\text{STO}} = 30^\circ$, respectively), the (114) planes on either side are tilted by half of this difference, and a GB angle of $\sim 3.5^\circ$ should be expected in the $\text{FeSe}_{0.5}\text{Te}_{0.5}$ films, which however is not observed in Figure 4(c). From Figures 4(c,d), the respective misorientation angles between domains were within 4° and 3° for in-plane and out-of-plane. The artificial GB (or rather the two sides of

the bicrystal) may be still recognized as a more macroscopic shift of the base line (average) misorientation (with respect to a common starting point) of $\sim 0.7^\circ$ out-of-plane and $\sim 0.9^\circ$ in-plane, which, however, is well within the range of domain-to-domain misorientations. Two more effects may explain that. First, the geometry coherency growth may happen again, now on (114) instead of (001), and since the c -axis of $\text{FeSe}_{0.5}\text{Te}_{0.5}$ is shorter than the single-layer distance in (114) direction in CeO_2 , the c -axis will tend towards the substrate normal, although just about negligible $\sim 0.1^\circ$. Secondly, since $\text{FeSe}_{0.5}\text{Te}_{0.5}$ single crystals typically grow in ab -oriented platelets, the surface energy of (001) may be concluded to be by far the lowest one. Hence, the system tends to adjust (001) parallel to the surface.

For the low-angle GBs, a similar combination of special GB in CeO_2 ($\Sigma 33[110]/\{441\}$ or $\Sigma 51[110]/\{551\}$ may be candidates), geometry coherency on the relevant, vicinal planes [(118) or (1110) for the above-mentioned GBs], and surface energy reduction may explain the FST GB angles being lower than expected.

3.3. Transport properties

The temperature dependence of the resistivity ρ of the inter- and intra-grain bridges is shown in Figure 5. Although $\text{FeSe}_{0.5}\text{Te}_{0.5}$ GBs were absent for $\theta_{\text{GB}}^{\text{STO}} = 24^\circ$ and 30° , the data for inter-grain were acquired from the

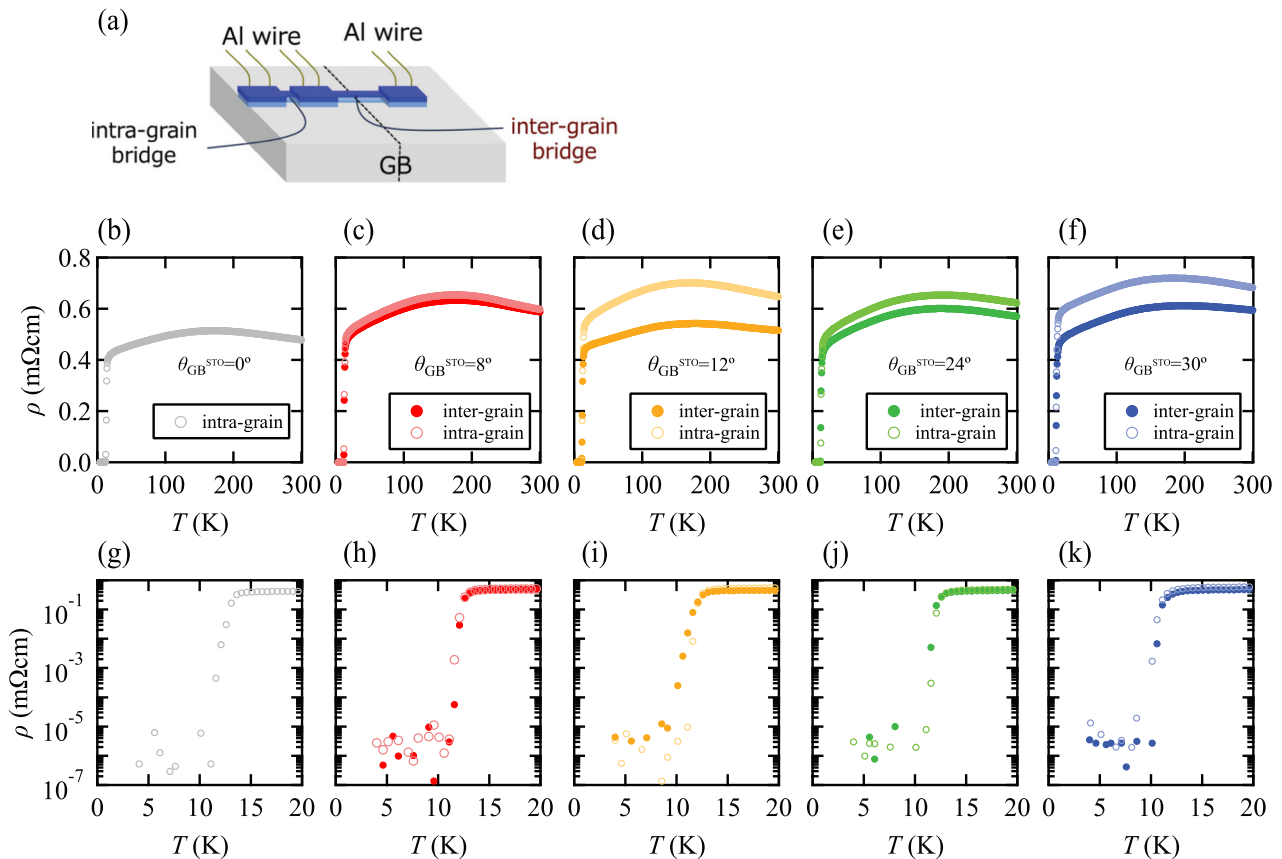


Figure 5. The electrical measurements using the intra- and inter-grain bridges is schematized in (a). The resistivity curves of the inter- and intra-grain bridges with various $\theta_{\text{GB}}^{\text{STO}}$ [(b)~(k)]. The open and solid symbols represent the intra- and inter-grain bridges, respectively. $\theta_{\text{GB}}^{\text{STO}} = 0^\circ$ [(b)] refers to the ordinary substrate. Semi-logarithmic plot of (b)~(f) in the vicinity of the transition [(g)~(k)].

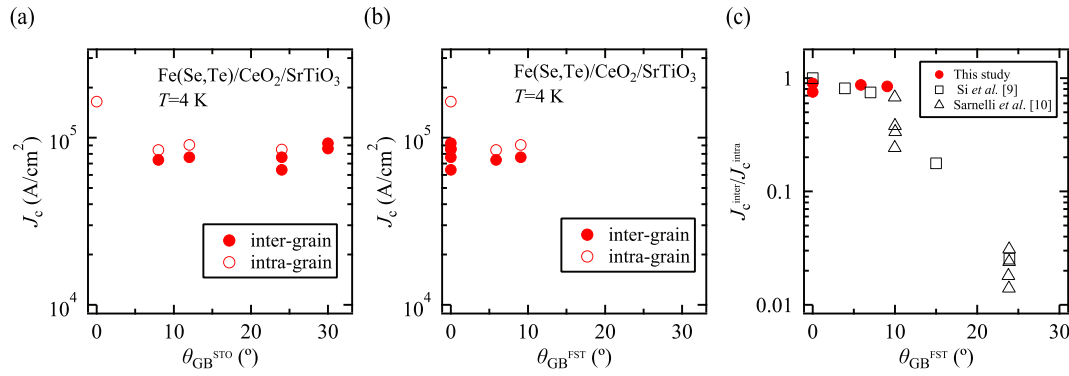


Figure 6. (a) J_c of the inter- and intra-grain bridges as a function of θ_{GB}^{STO} at 4 K. The micro-bridge with $\theta_{GB}^{STO}=0^\circ$ was fabricated from the film grown on the ordinary SrTiO₃ substrate. J_c was almost constant around 8×10^4 A/cm² except for the film grown on the ordinary SrTiO₃ substrate. (b) Data of (a) replotted as a function of θ_{GB}^{FST} . (c) The θ_{GB}^{FST} dependence of the normalized J_c for the Fe(Se,Te) bicrystal films measured at 4 K in comparison to data of [001]-tilt GBs (open symbols).

bridges located on the GB of CeO₂ and SrTiO₃. For $\theta_{GB}^{STO} \geq 24^\circ$, the normal state resistivity of the intra-grain bridges was somewhat higher than that of the inter-grain bridges. The semi-logarithmic plots of Figure 5(g,k) proved the resistivity dropped to the detection limit of the voltmeter below the transition. Additionally, the transition temperature of the intra-grain and the inter-grain bridges was almost the same for all samples.

Figure 6(a) shows the inter- and intra-grain J_c as a function of θ_{GB}^{STO} at 4.2 K. For $\theta_{GB}^{FST} = 0^\circ$, the micro-bridge was fabricated from the film grown on the ordinary SrTiO₃ substrate. All bridges showed a J_c of 8×10^4 A/cm² except for the bridge with $\theta_{GB}^{FST} = 0^\circ$ ($J_c = 1.6 \times 10^5$ A/cm²). The reason for higher J_c is that the only J_c component is the ab -plane. On the other hand, for $\theta_{GB}^{STO} > 0^\circ$, the inter- and intra-grain measurements contained two components of J_c : along the c -axis and the ab -plane. However, inter-grain J_c for the films having a $\theta_{GB}^{STO} = 24^\circ$ and 30° was $\sim 8 \times 10^4$ A/cm² (Figure 6(b)) although those films had a θ_{GB}^{FST} close to 0° , Figure 2(b). These results infer that the domain wall structure gave a negative impact on J_c . Additionally, the maximum in-plane misorientation was $\sim 3^\circ$ (Figure 4(d)), which also reduces J_c although the in-plane misorientation angles are less than the critical angle. In fact, the inter-grain J_c of the [001]-tilt GB in Fe(Se,Te) having a misorientation angle of 3° was reduced around 20% relative to the intra-grain J_c [9].

The ratio of inter-grain to intra-grain J_c as a function of θ_{GB}^{FST} is shown in Figure 6(c). The data for the [001]-tilt GB are also shown for comparison [9,10]. The ratio was almost 1 up to $\theta_{GB}^{FST} \sim 9.5^\circ$, which is similar to the [001]-tilt GBs. Hence, the absence of weak-link behavior also for [010]-tilt GBs up to $\sim 9.5^\circ$ is confirmed in FeSe_{0.5}Te_{0.5}.

4. Conclusion

FeSe_{0.5}Te_{0.5} thin films have been grown on CeO₂-buffered symmetric [010]-tilt roof-type SrTiO₃ bicrystal

substrates by pulsed laser deposition. Excess Fe was successfully removed by post-annealing at 200°C for 10 min in $pO_2 = 1$ Pa. The misorientation angle of the CeO₂ buffer layers and FeSe_{0.5}Te_{0.5} were different from those of the SrTiO₃ bicrystal substrates. The inclined growth of CeO₂ can be explained by the geometrical coherency model. For the nominal $\theta_{GB}^{STO} = 24^\circ$ and 30° [010]-tilt SrTiO₃ bicrystal substrates, domain wall boundaries rather than grain boundaries were formed in FeSe_{0.5}Te_{0.5} due to the epitaxial relation (001)[100] FeSe_{0.5}Te_{0.5} || (114)[22̄] CeO₂. The inter-grain J_c of the [010]-tilt GBs did not decay for a misorientation angle lower than 9.5° . The current results offer implications for mitigating the weak-link issue in HTS, since CeO₂ has been used as common buffer layers for HTS.

Disclosure statement

No potential conflict of interest was reported by the author(s).

Funding

This work was supported by JST CREST Grant Number [JPMJCR18J4]. This work was also partly supported by the Advanced Characterization Platform of the Nanotechnology Platform Japan sponsored by the Ministry of Education, Culture, Sports, Science and Technology (MEXT), Japan.

ORCID

Kazumasa Iida <http://orcid.org/0000-0003-1038-9630>
 Takafumi Hatano <http://orcid.org/0000-0002-6509-5835>
 Kai Walter <http://orcid.org/0009-0004-5366-6639>
 Bernhard Holzapfel <http://orcid.org/0000-0002-8420-4777>
 Jens Hänisch <http://orcid.org/0000-0003-2757-236X>
 Zimeng Guo <http://orcid.org/0000-0003-1332-2589>
 Satoshi Hata <http://orcid.org/0000-0001-6346-3422>

References

- [1] Fukuda Y, Kutsukake K, Kojima T, et al. Effects of grain boundary structure and shape of the solid-liquid interface on the growth direction of the grain boundaries in multicrystalline silicon. *Cryst Eng Comm.* 2022;24(10):1948–1954. doi: [10.1039/D1CE01573G](https://doi.org/10.1039/D1CE01573G)
- [2] Dimos D, Chaudhari P, Mannhart J, et al. Orientation dependence of grain-boundary critical currents in $\text{YBa}_2\text{Cu}_3\text{O}_{7-\delta}$ bicrystals. *Phys Rev Lett.* 1988;61(2):219–222. doi: [10.1103/PhysRevLett.61.219](https://doi.org/10.1103/PhysRevLett.61.219)
- [3] Hilgenkamp H, Mannhart J. Grain boundaries in high- T_c superconductors. *Rev Mod Phys.* 2002;74(2):485–549. doi: [10.1103/RevModPhys.74.485](https://doi.org/10.1103/RevModPhys.74.485)
- [4] Iida K, Hänisch J, Yamamoto A. Grain boundary characteristics of Fe-based superconductors. *Supercond Sci Technol.* 2020;33(4):043001. doi: [10.1088/1361-6668/ab73ef](https://doi.org/10.1088/1361-6668/ab73ef)
- [5] Held R, Schneider CW, Mannhart J, et al. Low-angle grain boundaries in $\text{YBa}_2\text{Cu}_3\text{O}_{7-\delta}$ with high critical current densities. *Phys Rev B.* 2009;79(1):014515. doi: [10.1103/PhysRevB.79.014515](https://doi.org/10.1103/PhysRevB.79.014515)
- [6] Goyal A, Field DP, Held R, et al. Grain boundary networks in high-performance, heteroepitaxial, YBCO films on polycrystalline, cube-textured metals. *Philos Mag Lett.* 2011;91(4):246–255. doi: [10.1080/09500839.2010.548345](https://doi.org/10.1080/09500839.2010.548345)
- [7] Zhu Y, Li Q, Tsay YN, et al. Structural origin of misorientation-independent superconducting behavior at [001] twist boundaries in $\text{Bi}_2\text{Sr}_2\text{CaCu}_2\text{O}_{8+\delta}$. *Phys Rev B.* 1998;57(14):8601–8608. doi: [10.1103/PhysRevB.57.8601](https://doi.org/10.1103/PhysRevB.57.8601)
- [8] Katase T, Ishimaru Y, Tsukamoto A, et al. Advantageous grain boundaries in iron-pnictide superconductors. *Nat Commun.* 2011;2(1):409. doi: [10.1038/ncomms1419](https://doi.org/10.1038/ncomms1419)
- [9] Si W, Zhang C, Shi X, et al. Grain boundary junctions of $\text{FeSe}_{0.5}\text{Te}_{0.5}$ thin films on SrTiO_3 bi-crystal substrates. *Appl Phys Lett.* 2015;106(3):032602. doi: [10.1063/1.4906429](https://doi.org/10.1063/1.4906429)
- [10] Sarnelli E, Nappi C, Camerlingo C, et al. Properties of Fe(Se, Te) bicrystal grain boundary junctions, Squids, and Nanostrips. *IEEE Trans Appl Supercond.* 2017;27:7400104. doi: [10.1109/TASC.2016.2636248](https://doi.org/10.1109/TASC.2016.2636248)
- [11] Omura T, Matsumoto T, Hatano T, et al. Fabrication of grain boundary junctions using NdFeAs (O, F) superconducting thin films. *J Phys Conf Ser.* 2018;1054:012024. doi: [10.1088/1742-6596/1054/1/012024](https://doi.org/10.1088/1742-6596/1054/1/012024)
- [12] Iida K, Omura T, Matsumoto T, et al. Grain boundary characteristics of oxypnictide NdFeAs(O,F) superconductors. *Supercond Sci Technol.* 2019;32(7):074003. doi: [10.1088/1361-6668/ab1660](https://doi.org/10.1088/1361-6668/ab1660)
- [13] Liu TJ, Ke X, Qian B, et al. Charge-carrier localization induced by excess Fe in the superconductor $\text{Fe}_{1+y}\text{Te}_{1-x}\text{Se}_x$. *Phys Rev B.* 2009;80(17):174509. doi: [10.1103/PhysRevB.80.174509](https://doi.org/10.1103/PhysRevB.80.174509)
- [14] Tokuta S, Hasegawa Y, Shimada Y, et al. Enhanced critical current density in K-doped Ba122 polycrystalline bulk superconductors via fast densification. *iScience.* 2022;25(4):103992. doi: [10.1016/j.isci.2022.103992](https://doi.org/10.1016/j.isci.2022.103992)
- [15] Tokuta S, Yamamoto A. Enhanced upper critical field in Co-doped Ba122 superconductors by lattice defect tuning. *APL Mater.* 2019;7(11):111107. doi: [10.1063/1.5098057](https://doi.org/10.1063/1.5098057)
- [16] Si W, Han S, Shi X, et al. High current superconductivity in $\text{FeSe}_{0.5}\text{Te}_{0.5}$ -coated conductors at 30 tesla. *Nat Commun.* 2013;4(1):1347. doi: [10.1038/ncomms2337](https://doi.org/10.1038/ncomms2337)
- [17] Ozaki T, Wu L, Zhang C, et al. A route for a strong increase of critical current in nanostrained iron-based superconductors. *Nat Commun.* 2016;7(1):13036. doi: [10.1038/ncomms13036](https://doi.org/10.1038/ncomms13036)
- [18] Zhang C, Si W, Li Q. Doubling the critical current density in superconducting $\text{FeSe}_{0.5}\text{Te}_{0.5}$ thin films by low temperature oxygen annealing. *Appl Phys Lett.* 2016;109(20):202601. doi: [10.1063/1.4967879](https://doi.org/10.1063/1.4967879)
- [19] Sun Y, Shi Z, Tamegai T. Review of annealing effects and superconductivity in $\text{Fe}_{1+y}\text{Te}_{1-x}\text{Se}_x$ superconductors. *Supercond Sci Technol.* 2019;32(10):103001. doi: [10.1088/1361-6668/ab30c2](https://doi.org/10.1088/1361-6668/ab30c2)
- [20] Rauch EF, Portillo J, Nicolopoulos S, et al. Automated nanocrystal orientation and phase mapping in the transmission electron microscope on the basis of precession electron diffraction. *Z für Kristallogr.* 2010;225(2–3):103–109. doi: [10.1524/zkri.2010.1205](https://doi.org/10.1524/zkri.2010.1205)
- [21] Guo Z, Gao H, Kondo K, et al. Nanoscale texture and microstructure in a NdFeAs(O,F)/IBAD-MgO superconducting thin film with superior critical current properties. *ACS Appl Electron Mater.* 2021;3(7):3158–3166. doi: [10.1021/acsaelm.1c00364](https://doi.org/10.1021/acsaelm.1c00364)
- [22] Zhang N, Liu C, Zhao J-L, et al. Observation of selective surface element substitution in $\text{FeTe}_{0.5}\text{Se}_{0.5}$ superconductor thin film exposed to ambient air by synchrotron radiation spectroscopy. *Chin Phys B.* 2016;25(9):097402. doi: [10.1088/1674-1056/25/9/097402](https://doi.org/10.1088/1674-1056/25/9/097402)
- [23] Mukasa K, Matsuura K, Qiu M, et al. High-pressure phase diagrams of $\text{FeSe}_{1-x}\text{Te}_x$: correlation between suppressed nematicity and enhanced superconductivity. *Nat Commun.* 2021;12(1):381. doi: [10.1038/s41467-020-20621-2](https://doi.org/10.1038/s41467-020-20621-2)
- [24] Popov R, Ackermann K, Rijckaert H, et al. Effect of oxygenation process on flux pinning in pristine and BaHfO_3 nanocomposite $\text{GdBa}_2\text{Cu}_3\text{O}_7$ superconducting thin films. *J Phys: Conf Ser.* 2020;1559(1):012038. doi: [10.1088/1742-6596/1559/1/012038](https://doi.org/10.1088/1742-6596/1559/1/012038)
- [25] Nagai H. Structure of vapor-deposited $\text{Ga}_x\text{In}_{1-x}$ crystals. *J Appl Phys.* 1974;45(9):3789–3794. doi: [10.1063/1.1663861](https://doi.org/10.1063/1.1663861)
- [26] Ayers JE, Ghandhi SK, Schowalter LJ. Crystallographic tilting of heteroepitaxial layers. *J Cry Growth.* 1991;113(3–4):430–440. doi: [10.1016/0022-0248\(91\)90077-1](https://doi.org/10.1016/0022-0248(91)90077-1)
- [27] Budai JD, Yang W, Tamura N, et al. X-ray microdiffraction study of growth modes and crystallographic tilts in oxide films on metal substrates. *Nature Mater.* 2003;2(7):487–492. doi: [10.1038/nmat916](https://doi.org/10.1038/nmat916)
- [28] Bryja H, Hühne R, Iida K, et al. Deposition and properties of Fe(Se,Te) thin films on vicinal CaF_2 substrates. *Supercond Sci Technol.* 2017;30(11):115008. doi: [10.1088/1361-6668/aa8421](https://doi.org/10.1088/1361-6668/aa8421)
- [29] Kaneko S, Akiyama K, Ito T, et al. Large lattice misfit on epitaxial thin film: coincidence site lattice expanded on polar coordinate system. *Jpn J Appl Phys.* 2010;49(8S1):08JE02. doi: [10.1143/JJAP.49.08JE02](https://doi.org/10.1143/JJAP.49.08JE02)
- [30] Lucid AK, Plunkett AC, Watson GW. Predicting the structure of grain boundaries in fluorite-structured materials. *Johnson Matthey Technol Rev.* 2019;63(4):247–254. doi: [10.1595/205651319X15598975874659](https://doi.org/10.1595/205651319X15598975874659)
- [31] Feng B, Sugiyama I, Hojo H, et al. Atomic structures and oxygen dynamics of CeO_2 grain boundaries. *Sci Rep.* 2016;6(1):20288. doi: [10.1038/srep20288](https://doi.org/10.1038/srep20288)

Supplementary information on “Structural analysis and transport properties of the [010]-tilt grain boundaries in Fe(Se,Te)”

Kazumasa Iida^{1,8}, Yoshihiro Yamauchi², Takafumi Hatano^{2,8}, Kai Walter³, Bernhard Holzapfel³, Jens Hänisch³, Zimeng Guo^{4,8}, Hongye Gao⁵, Haoshan Shi⁶, Shinnosuke Tokuta^{7,8}, Satoshi Hata^{4,5,6,8}, Akiyasu Yamamoto^{7,8}, Hiroshi Ikuta^{2,9}

1 College of Industrial Technology, Nihon University, 1-2-1 Izumi-cho, Narashino, Chiba 275-8575, Japan;

2 Department of Materials Physics, Nagoya University, Furo-cho, Nagoya 464-8603, Japan;

3 Institute for Technical Physics, Karlsruhe Institute of Technology, Hermann-von-Helmholtz-Platz 1, Eggenstein-Leopoldshafen, 76344, Germany;

4 Department of Advanced Materials Science and Engineering, Kyushu University, Kasuga, Fukuoka 816-8580, Japan;

5 The Ultramicroscopy Research Center, Kyushu University, Motooka, Fukuoka 819-0395, Japan;

6 Interdisciplinary Graduate School of Engineering Sciences, Kyushu University, Kasuga, Fukuoka 816-8580, Japan;

7 Department of Applied Physics, Tokyo University of Agriculture and Technology, Koganei, Tokyo 184-8588, Japan;

8 JST CREST, Kawaguchi, Saitama 332-0012, Japan;

9 Research Center for Crystalline Materials Engineering, Nagoya University, Furo-cho, Nagoya 464-8603, Japan

CONTACT Kazumasa Iida: iida.kazumasa@nihon-u.ac.jp

1. X-ray reflectivity measurement for CeO₂ grown on SrTiO₃(001)

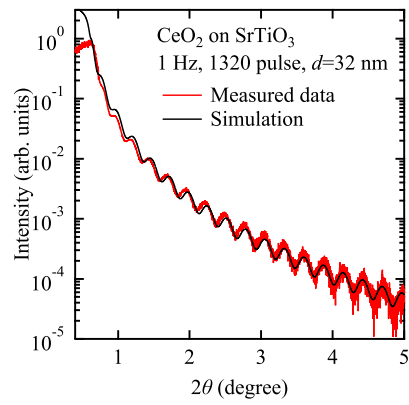


Figure S1 | X-ray reflectivity measurement confirmed that the thickness of CeO₂ is 32 nm, which is almost identical to the one measured from the cross-sectional ADF-STEM image [fig. 3(a)].

2. The 101 reflection of ϕ scans and the 00 l rocking curves of FeSe_{0.5}Te_{0.5} grown on the CeO₂-buffered SrTiO₃ ordinary substrate and bicrystal substrate with $\theta_{GB}^{STO}=30^\circ$.

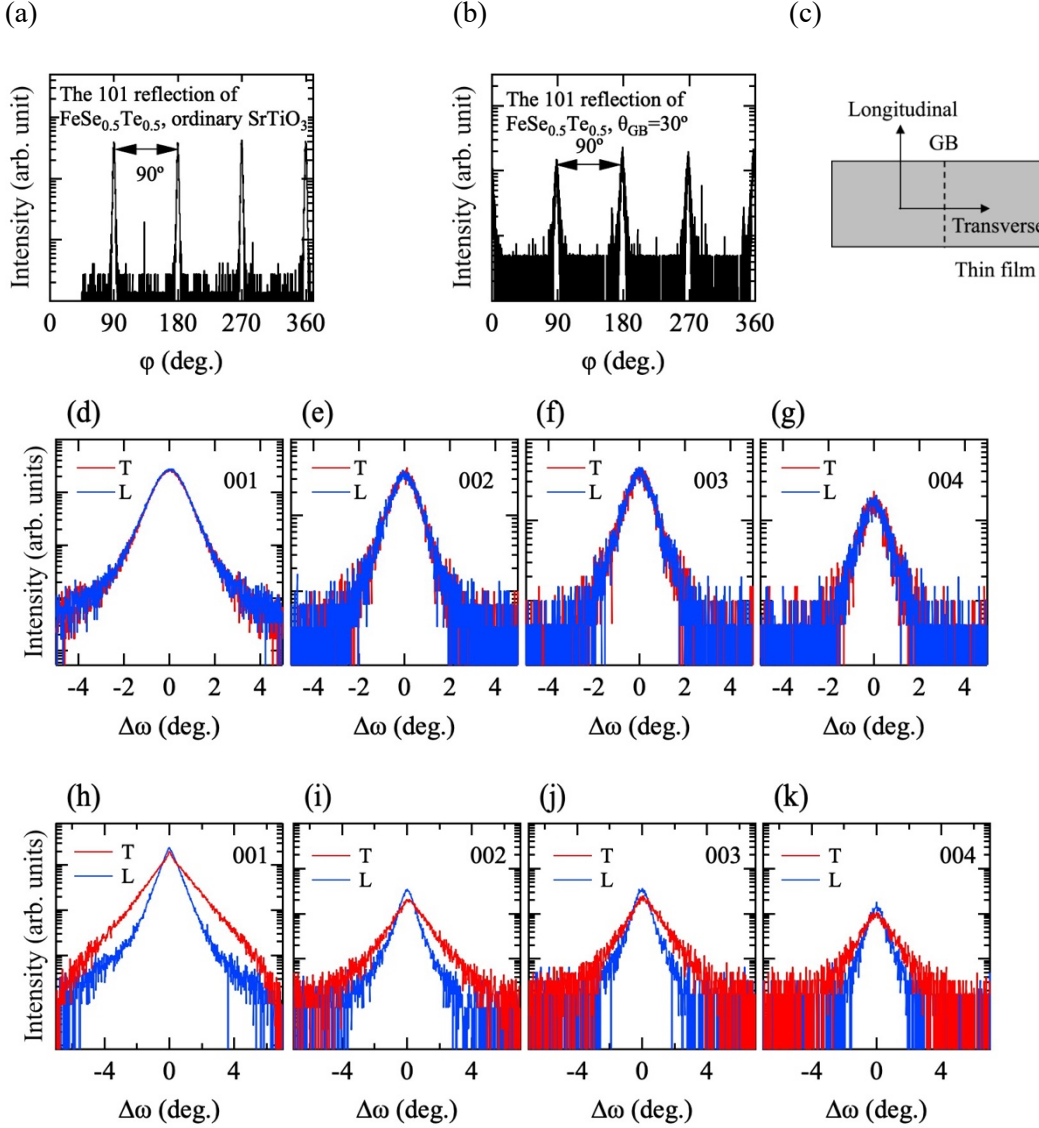


Figure S2 | (a) The ϕ scans of the 101 reflection of FeSe_{0.5}Te_{0.5} grown on CeO₂-buffered ordinary SrTiO₃ substrate and (b) bicrystal substrate with $\theta_{GB}^{STO}=30^\circ$. (c) The schematic illustration of the X-ray scan direction for the 00 l rocking curves. (d)-(g) The 00 l ($l=1, 2, 3$ and 4) rocking curves of FeSe_{0.5}Te_{0.5} grown on CeO₂-buffered ordinary SrTiO₃ substrate. “T” and “L” denote the transverse and longitudinal directions of the X-ray scans, shown in (c). As expected, no difference in FWHM were observed. On the other hand, for the film grown on bicrystal substrate ($\theta_{GB}^{STO}=30^\circ$), the FWHM for “T” (i.e., perpendicular to the GB) are larger than those for “L” [(h)~(k)].

Table S1 shows the FWHM exhibited in fig. S2(a) and (b). The $\Delta\phi$ of the $\text{FeSe}_{0.5}\text{Te}_{0.5}$ film on single crystal SrTiO_3 ($\theta_{\text{GB}}^{\text{STO}} = 0^\circ$) is smaller than of the film on bicrystal substrate. Table S2 summarizes the crystalline quality of the out-of-plane direction of the $\text{FeSe}_{0.5}\text{Te}_{0.5}$ films on single crystal and bicrystal substrates. The FWHM of $\text{FeSe}_{0.5}\text{Te}_{0.5}$ on ordinary SrTiO_3 are almost the same values regardless of the scan directions. On the other hand, for $\text{FeSe}_{0.5}\text{Te}_{0.5}$ on bicrystal substrate, FWHM shows a strong directional dependence: FWHM of “T”-direction are always larger than those of “L”-direction.

Table S1| The FWHM ($\Delta\phi$) of $\text{FeSe}_{0.5}\text{Te}_{0.5}$ grown on the CeO_2 -buffered ordinary SrTiO_3 substrate and bicrystal SrTiO_3 substrate ($\theta_{\text{GB}}^{\text{STO}}=30^\circ$).

$\text{FeSe}_{0.5}\text{Te}_{0.5}$ on	$\Delta\phi_{101}$ ($^\circ$)	$\Delta\phi_{011}$ ($^\circ$)	$\Delta\phi_{\bar{1}01}$ ($^\circ$)	$\Delta\phi_{0\bar{1}1}$ ($^\circ$)
ordinary SrTiO_3	2.20	2.24	2.15	2.28
bicrystal SrTiO_3 ($\theta_{\text{GB}}^{\text{STO}}=30^\circ$)	3.82	3.95	3.82	4.07

Table S2| The FWHM ($\Delta\omega$) of $\text{FeSe}_{0.5}\text{Te}_{0.5}$ grown on the CeO_2 -buffered ordinary SrTiO_3 substrate and bicrystal SrTiO_3 substrate ($\theta_{\text{GB}}^{\text{STO}}=30^\circ$).

$\text{FeSe}_{0.5}\text{Te}_{0.5}$ on	direction	$\Delta\omega_{001}$ ($^\circ$)	$\Delta\omega_{002}$ ($^\circ$)	$\Delta\omega_{003}$ ($^\circ$)	$\Delta\omega_{004}$ ($^\circ$)
ordinary SrTiO_3	T	1.26	1.15	1.15	1.13
	L	1.25	1.16	1.13	1.07
bicrystal SrTiO_3 ($\theta_{\text{GB}}^{\text{STO}}=30^\circ$)	T	2.73	2.27	1.64	1.59
	L	1.19	0.83	0.87	0.91

2. Vicinal angle evaluated from the geometrical coherency model

To evaluate vicinal angles of $\text{FeSe}_{0.5}\text{Te}_{0.5}$ grown on off-cut CaF_2 substrates, the following equation is employed:

$$\Delta\theta_{\text{vic}}^{\text{FST}} = \left| \tan^{-1} \left(\frac{d_{\text{CaF}_2} - d_{\text{FST}}}{d_{\text{CaF}_2}} \tan\theta_{\text{vic}}^{\text{CaF}_2} \right) \right| \quad (\text{S1})$$

with

$$\theta_{\text{vic}}^{\text{FST}} = \Delta\theta_{\text{vic}}^{\text{FST}} + \theta_{\text{vic}}^{\text{CaF}_2} \quad (\text{S2})$$

where $\theta_{\text{vic}}^{\text{FST}}$ is the vicinal angle of $\text{FeSe}_{0.5}\text{Te}_{0.5}$, d_{CaF_2} is the lattice parameter of CaF_2 (5.462 Å), d_{FST} is the c -axis length of $\text{FeSe}_{0.5}\text{Te}_{0.5}$ (5.96 Å) [S1] and $\theta_{\text{vic}}^{\text{CaF}_2}$ is the vicinal angle of the CaF_2 substrates. Due to $d_{\text{FST}} > d_{\text{CaF}_2}$, the direction of the tilt of [001] $\text{FeSe}_{0.5}\text{Te}_{0.5}$ from [001] CaF_2 is away from the substrate normal. The $\text{FeSe}_{0.5}\text{Te}_{0.5}$ thin films were grown on off-cut CaF_2 substrates at 260 °C and 400 °C, respectively [S2]. Figure S3 shows the measured vicinal angle of $\text{FeSe}_{0.5}\text{Te}_{0.5}$ by X-ray diffraction as a function of $\theta_{\text{vic}}^{\text{CaF}_2}$. The dashed lines are calculation from equations S1 and S2. As can be seen, the vicinal angles of $\text{FeSe}_{0.5}\text{Te}_{0.5}$ grown at 260 °C deviate

from the calculation, whereas they lie on the calculated lines for the films grown at 400 °C. These results suggest that the inclined growth mechanism based on the geometrical coherence model is operative at high growth temperature, but not at low growth temperature.

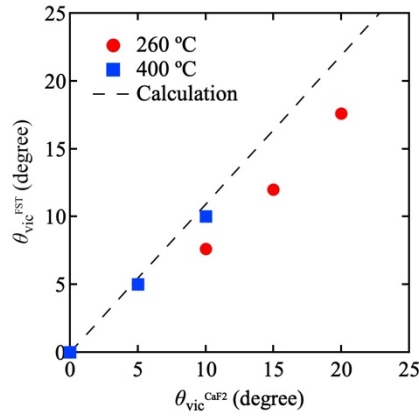


Figure S3 | The vicinal angle of $\text{FeSe}_{0.5}\text{Te}_{0.5}$ on off-cut CaF_2 substrates grown at 260 °C and 400 °C as a function of $\theta_{\text{vic}}^{\text{CaF}_2}$.

4. Cross-sectional TEM image of $\text{FeSe}_{0.5}\text{Te}_{0.5}$ on CeO_2 -buffered ordinary SrTiO_3 substrate

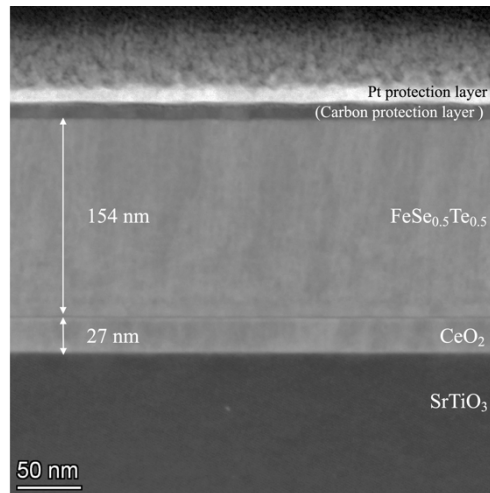


Figure S4 | The cross-sectional view of $\text{FeSe}_{0.5}\text{Te}_{0.5}$ grown on the CeO_2 -buffered SrTiO_3 substrate ($\theta_{\text{GB}}^{\text{STO}} = 0^\circ$) obtained by ADF-STEM.

Reference

- [S1] Musaka K, Matsuura K, Qin M, Saito M, Sugiura Y, Ishida K, Otani M, Oishi Y, Mizukami Y, Hashimoto K, Gouchi J, Kumai R, Uwatoko Y, Shibauchi T. High-pressure phase diagrams of $\text{FeSe}_{1-x}\text{Te}_x$: correlation between suppressed nematicity and enhanced superconductivity. *Nat. Commun.* (2021);12: 381. doi: 10.1038/s41467-020-20621-2
- [S2] Bryja H, Hühne R, Iida K, Molata S, Sala A, Putti M, Schultz L, Nielsch K, Hänisch J.

Deposition and properties of Fe(Se,Te) thin films on vicinal CaF₂ substrates. Supercond. Sci. Technol. 2017; 30: 115008. doi: 10.1088/1361-6668/aa8421